Arsenic *K*-edge and Thallium *L3*-edge XANES, with XFM imaging and LA-ICP-MS to determine oxidation states and distribution in sphalerite

Christopher H. Ingles [a,*], John A. Mavrogenes [a], Nicholas D. Tailby [b], Jeremy L. Wykes [c]

[a] *Research School of Earth Sciences, Australian National University, 142 Mills Rd, Acton, ACT, Australia 0200*
[b] *Division of Earth Science, School of Environmental and Rural Science, University of New England, Armidale, NSW, Australia 2351*
[c] *Australian Synchrotron, Australian Nuclear Science and Technology Organisation, 800 Blackburn Rd, Clayton, VIC, Australia 3168*

ARTICLE INFO

ABSTRACT

XANES, XFM imaging and LA-ICP-MS were employed to reveal the localisation of elements and the oxidation states of As and Tl in highly banded MVT sphalerite from Wiesloch, Germany. Arsenic *K*-edge and Tl *L3*-edge XANES spectra were retrieved, and results were compared to reference standards that represented different oxidation states. Fingerprinting analyses indicated As^{3+} and Tl^+ in the Wiesloch sphalerite. Substitution mechanisms are provided that include the coupled incorporation of As and Tl in sphalerite, and a two-step series of reactions that creates and consumes vacant cation sites to better accommodate the larger size of Tl^+ in tetrahedral coordination. XANES spectra also revealed a different edge position for As in Porgera (Papua New Guinea) pyrite and XFM imaging showed As localised entirely in the pyrite, rather than the adjacent sphalerite. A pH sensitive measure of redox in sphalerite-pyrite coprecipitated mineral assemblages is therefore suggested.

1. Introduction

Despite their toxic reputations, As and Tl are important elements that have numerous uses in industrial and medical applications. Arsenic compounds are used in the manufacturing of semiconductor microchips, infrared materials and batteries (George, 2023). Thallium is found in medical imaging devices, as well as radiation detection equipment and high-temperature superconductors (Singh, 2022). The increasing demand for 21st century technologies, furthermore, has resulted in As being placed on US, European and Australian critical supply lists, while Tl stockpiles are dwindling rapidly (Burton, 2022; Grohol and Veeh, 2023; King, 2023).

Arsenic is mainly found in realgar (As_4S_4) and orpiment (As_2S_3), in association with low-temperature hydrothermal ores (Tabelin and Igarishi, 2009). Thallium is primarily recovered from sulfides, including pyrite (FeS_2), carlinite (Tl_2S) and lorándite ($TlAsS_2$). Arsenic and Tl share similar geochemistries (Zhao and Gu, 2021; Dordevic et al., 2021), with both elements, for example, used as indicators for Carlin-style gold deposits (Rytuba, 1986; Ikramuddin et al., 1986).

Sphalerite (ZnS), a sulfide found in a variety of deposit types, is the world's chief Zn source. Numerous elements are retrieved from sphalerite, including critical metals In, Ga, Ge, Mn and Sb (Cook et al., 2009).

Arsenian sphalerite from the Alacrán deposit in Chile contains up to 2 wt % As (Clark, 1970). Thallium can also be concentrated within sphalerite and as a result, the treatment of Zn ore is the primary source of environmental Tl pollution (Karbowska et al., 2014; Zhou et al., 2022).

Sphalerite often displays colloform growth patterns, sector zoning and alternating bands of variable metal contents. Schalenblende is an example of colourful banding attributed to sphalerite and the anion deficient wurtzite polymorph (eg: Mavrogenes et al., 1992). The complexity of sphalerite is further seen in textures known as 'chalcopyrite disease', which were once thought to be the result of exsolution however are likely the result of diffusion induced segregation (DIS), despite the diffusing elements not being controlled by concentration gradients (Barton and Bethke, 1987; Govindarao et al., 2018).

Many aspects of substitution mechanisms in sphalerite could be better understood, including how, why and where each element resides in the cubic lattice. Equations governing the incorporation of metals into sphalerite are contentious, as they require agreement on oxidation states and coupled substitutions. Furthermore, the large crystal radius of cations such as Ag^+ (1.14 Å; Shannon, 1976), also complicate substitutions, particularly when determining which elements are in tetrahedral coordination in solid solution with Zn^{2+} (0.74 Å; Shannon, 1976), and which are instead hosted in micro- or nano-inclusions of other minerals (Ye
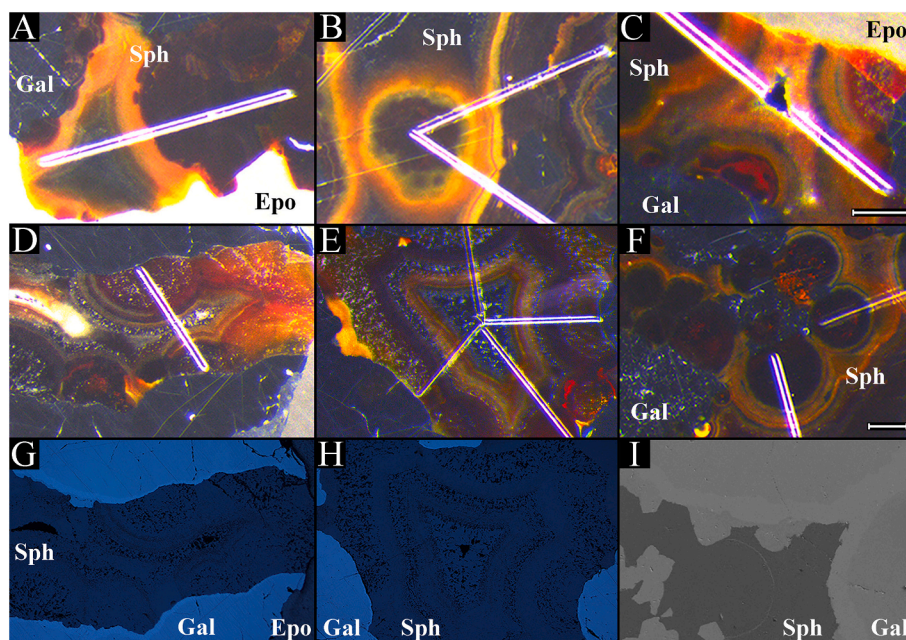

Fig. 1. Photomicrographs from WIES1 (A), WIES2 (B and D) and WIES3 (C, E and F). Reflected light images (G and H) are the same sphalerites as D and E respectively. Back Scattered Electron image (I). A, B, C and I share a scale bar (250 μm). D, E, F, G and H share a scale bar (250 μm). Laser ablation traverses are visible in A through F. Sph = sphalerite, Gal = galena, Epo = epoxy.

Table 1
Arsenic and Tl samples and standards prepared for XANES.

	Mineral	Formula	As Oxidation state	Tl Oxidation state	Origins
Samples	Sphalerite	ZnS	Unknown	Unknown	Wiesloch, Germany
	Arsenian Pyrite	FeS$_2$	Unknown	–	Porgera, Papua New Guinea
Standards	Realgar	As$_4$S$_4$	+2	–	La Polomo, Peru
	Orpiment	As$_2$S$_3$	+3	–	Nevada, USA
	Mimetite	Pb$_5$(AsO$_4$)$_3$Cl	+5	–	Ojuela, Mexico
	Lorándite	TlAsS$_2$	–	+1	Allchar, Macedonia
	Tl-Silicate	Tl$_4$Si$_5$O$_{12}$	–	+1	Synthesised at RSES, ANU

Table 2
Median EDX and LA-ICP-MS concentrations for WIES1–3. All values presented in ppm, except Zn and S.

	Zn (wt%)	S (wt%)	Mn	Fe	Co	Cu	Ge	As	Cd	Sb	Tl	Pb
WIES1	62.6	31.3	10.5	491.5	0.6	2.5	30.1	8520.4	690.4	3510.7	6001.2	22,495.2
WIES2	64.3	31.3	7.4	271.1	0.7	2.8	27.8	8135.0	776.5	2973.2	6061.9	19,765.0
WIES3	64.9	31.7	5.5	187.3	0.6	2.5	18.3	2605.0	1382.3	2958.8	4434.2	15,411.6

et al., 2011). Oxidation states greatly affect the radii and chemical behaviour of a given element. For example, Tl$^+$ is considerably more fatal to humans than Tl^{3+}, due to its ability to follow K$^+$ pathways through the human body (Yu et al., 2016).

The sphalerite lattice is versatile and has been shown to incorporate a range of elemental concentrations over a range of environmental conditions. This led to a proposed thermo-barometer (Scott and Barnes, 1971; Scott, 1973) and the use of sphalerite as an indicator for ore types (Frenzel et al., 2016). The sphalerite lattice has also been shown to be cation deficient (Scott and Barnes, 1972), increase in size with higher Fe concentrations (eg: Wright and Gale, 2010; Chareev et al., 2017), and accommodate larger cations than expected (Pring et al., 2008).

X-ray Absorption Near Edge Structure (XANES) is a non-destructive, microanalytical technique that can be used to determine the electronic structures of atoms bound within a crystal lattice. The technique has numerous advantages over conventional techniques (eg: EPMA, LA-ICP-MS, *etc.*) in that it can provide information about valence speciation and site occupancy (including both coordination and site distortion under

specific circumstances) over a micron-scale analytical volume. Previous examples of successful XANES fingerprinting include studies showing evidence of Cu$^+$, Fe^{2+} and Ge^{4+} in sphalerite (Cook et al., 2012; Belissont et al., 2016), and As^{2+} and As^{3+} in realgar and orpiment respectively (Le Pape et al., 2018).

The goal of the present study was to use XANES to determine the oxidation states of As and Tl in sphalerite and assess their substitution mechanisms. Sphalerite from Wiesloch, Germany, was chosen for analysis, which has been reported to contain elevated concentrations of As and Tl (Pfaff et al., 2011).

2. Materials and methods

2.1. Samples

The sphalerite in this study was obtained from the Wiesloch mining area, Baden-Württemberg, Germany. Wiesloch was mined for more than 2000 years and is known as a high concentration resource of Tl, As, Sb
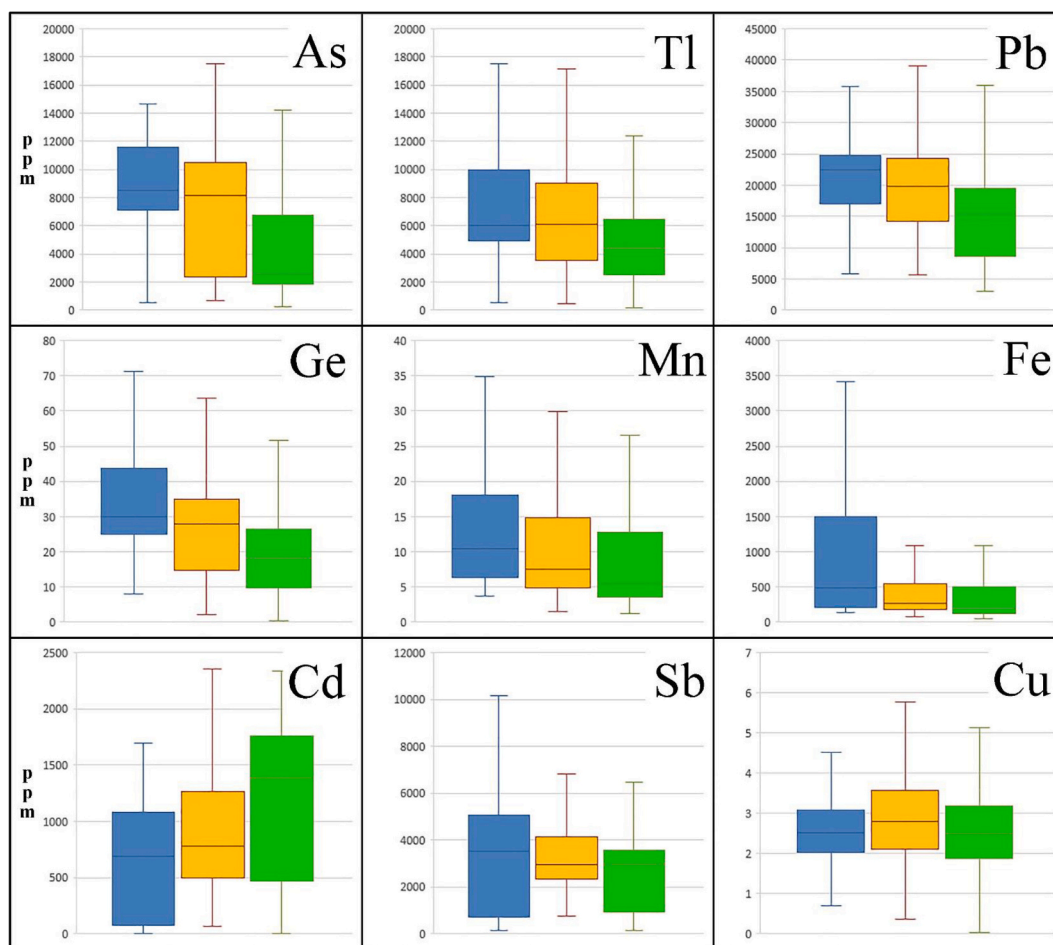
Fig. 2. Box and whiskers plot of LA-ICP-MS minor and trace element concentrations in WIES1 (blue), WIES2 (orange) and WIES3 (green). The bottom and top of each box represent the 25th and 75th percentiles respectively, with horizontal lines inside each box showing median values. The whiskers extend downwards and upwards to the 5th and 95th percentiles respectively. (For interpretation of the references to colour in this figure legend, the reader is referred to the web version of this article.)

Table 3
SEM results (wt%) from WIES2. Traverse from the galena, through the reaction rim and into the sphalerite. Results normalised to 100 wt% for comparison. Concentrations not included were below detection limits (0.1 wt%).

	Zn	S	Fe	Cd	As	Tl	Sb	Pb
Galena	–	17.25	–	–	7.59	–	4.21	70.95
Galena	–	17.63	–	–	7.21	–	4.35	70.82
Galena	–	17.61	–	–	7.60	–	3.79	71.00
Reaction rim	–	14.14	–	–	–	–	3.68	82.18
Reaction rim	0.44	14.02	–	–	0.23	–	3.73	81.59
Reaction rim	1.78	13.84	–	–	–	–	3.29	81.08
Sphalerite	64.55	31.56	0.15	0.24	1.08	–	–	2.42
Sphalerite	64.49	32.17	–	–	1.06	–	0.34	1.95
Sphalerite	64.14	31.04	0.18	–	1.01	1.29	–	2.33
Sphalerite	63.92	31.34	0.17	–	1.26	1.13	–	2.18

and Cd in remnant MVT tailings across the region (Stüben et al., 2001; Pfaff et al., 2010).

Colloform sphalerite revealed bands alternating between shades of orange, brown, red, yellow and grey (Fig. 1), which match the description of low temperature, high-As, high-Tl Wiesloch sphalerite of Pfaff et al. (2011). Three pieces of Wiesloch ore, each 1×1 cm, were mounted in 1-in. polished epoxy blocks labelled WIES1 to 3. Galena was adjacent to each sphalerite, with WIES2 and WIES3 displaying reaction rims between the two phases (Fig. 1G and I). Realgar, orpiment and mimetite ($Pb_5(AsO_4)_3Cl$) standards were chosen for XANES, to represent di-, tri- and penta-valent As oxidation states respectively. Previously

measured As K-edge XANES spectra were also included for comparison, including cobaltite (CoAsS), arsenopyrite (FeAsS), tennantite ($Cu_{12}As_4S_{13}$), enargite (Cu_3AsS_4), arsenolite (As_4O_6), sodium arsenite ($NaAsO_2$), sodium arsenate (Na_3AsO_4) and scorodite ($FeAsO_4.2H_2O$) (Di Benedetto et al., 2011; Diacomanolis et al., 2017; Schoepfer et al., 2024).

Thallium standards measured by XANES were both monovalent and consisted of lorándite and a Tl-silicate ($Tl_4Si_5O_{12}$) synthesised at the Research School of Earth Sciences (RSES) at the Australian National University (ANU). Additional Tl $L3$-edge spectra were also included for analysis from thallium(I) chloride (TlCl), thallium carbonate (Tl_2CO_3),
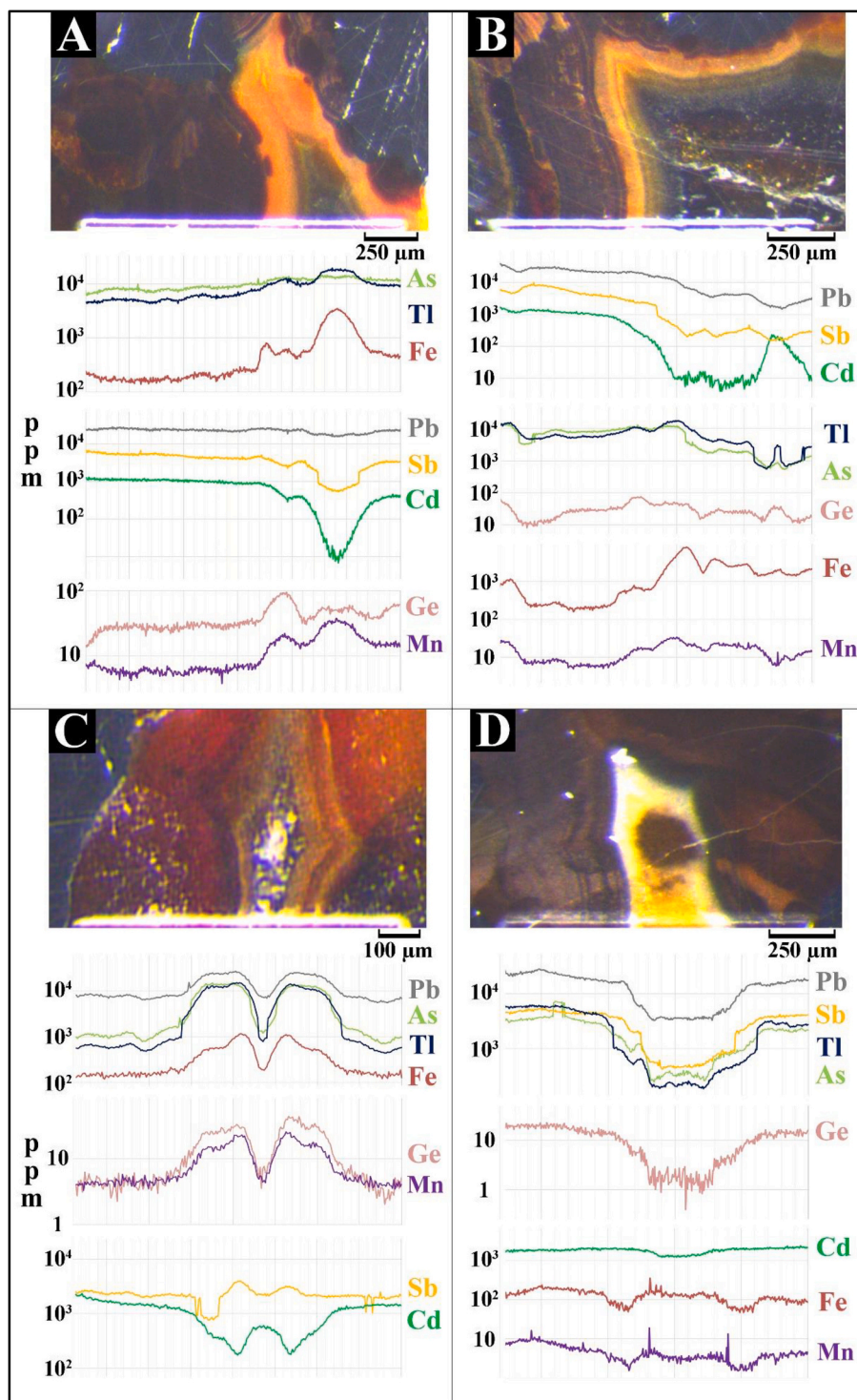
Fig. 3. LA-ICP-MS concentrations aligned to stereoscopic images of traverses and sphalerite bands in WIES1 (A and B), WIES2 (C) and WIES3 (D).

aqueous Tl(I) solution, aqueous Tl(III) solution, avicennite (Tl$_2$O$_3$), thallium(III) trifluoroacetate (Tl(CF$_3$COO)$_3$) and Tl$_2$Ba$_2$O$_5$ (Agarwal and Vishnoi, 2005; Garrido et al., 2020; Łyczko et al., 2023). All synchrotron standards were ground and diluted with cellulose to 5000 ppm, before being prepared into 1 cm pellets and sealed with Kapton tape. A coprecipitated mineral assemblage of sphalerite and arsenian pyrite was also included for X-ray Fluorescence Microscopy (XFM) and As in pyrite was later analysed by XANES. A summary of samples and standards prepared for XANES is presented as Table 1.

2.2. Methodology.

2.2.1. Energy dispersive spectroscopy

Energy Dispersive X-ray (EDX) analyses were undertaken to quantify major and minor element concentrations in the samples and XANES standards. The Hitachi 4300 SE/N Schottky Field Emission - Scanning Electron Microscope (FE-SEM) is standardised with a Faraday cup and housed in the Centre for Advanced Microscopy at the ANU.
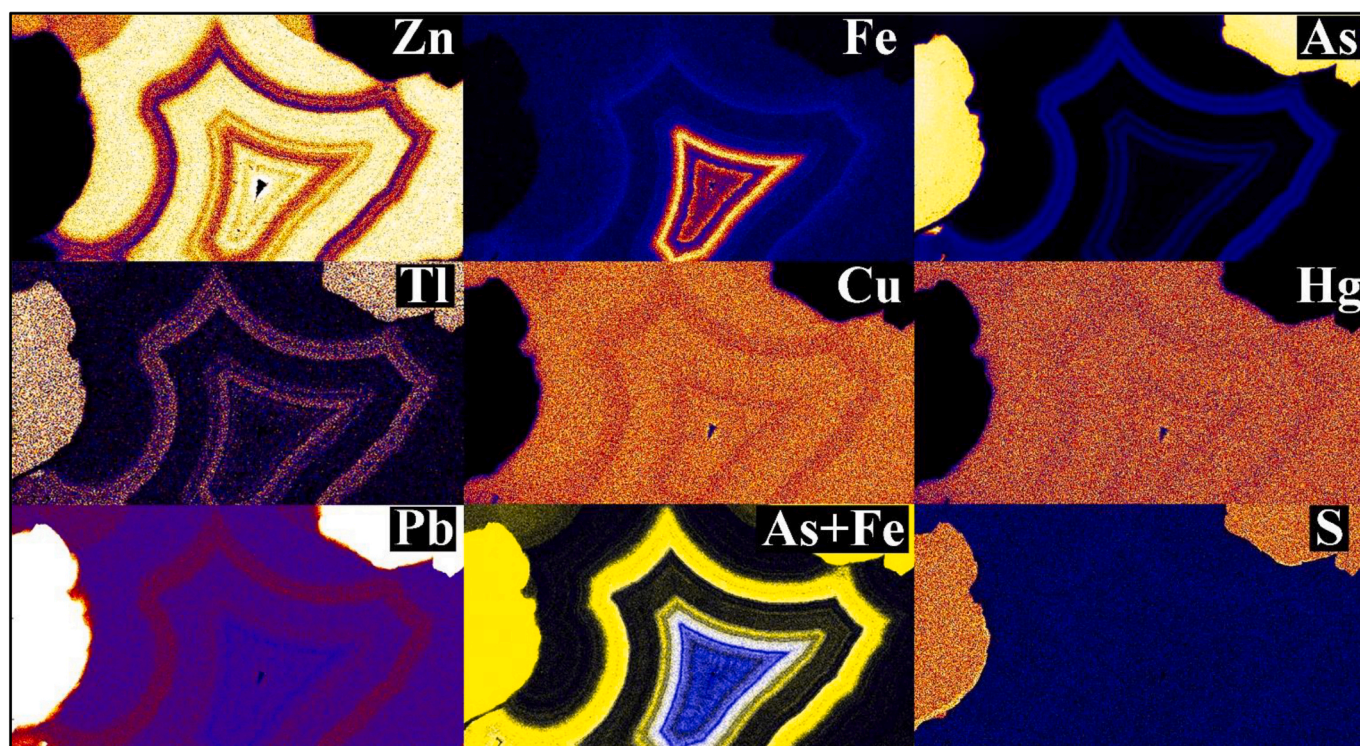
Fig. 4. XFM images showing Zn, Fe, As, Tl, Cu, Hg, Pb and S concentrations in sphalerite bands in WIES3. Warmer colours represent higher concentrations. As+Fe is an RGB composite image, depicting the highest As concentrations in yellow and Fe in blue. Galena is visible in all images at the left and top right in each frame (most visible in Pb, As and S images). Horizontal scale of 2 mm for each image. (For interpretation of the references to colour in this figure legend, the reader is referred to the web version of this article.)

2.2.2. Laser ablation – inductively coupled plasma – mass spectrometry

Laser Ablation – Inductively Coupled Plasma – Mass Spectrometry (LA-ICP-MS) traverses were employed to measure trace element concentrations *in situ* across sphalerite zones. The LA-ICP-MS system is in the RSES at the ANU and is comprised of a Coherent Compex110 193 nm ArF excimer laser coupled to a HelEx dual-volume sample cell and Agilent 7700× Q-ICP-MS. The laser was operated at 80 mj/pulse and 5 Hz, with a circular mask of 28 μm to give a laser fluence at the sample of 1–2 J/cm^2. The mass sweep measured by the LA-ICP-MS ranged from light (34) to heavy (209), and included masses corresponding to the following: ^{34}S, ^{45}Sc, ^{47}Ti, ^{51}V, ^{52}Cr, ^{55}Mn, ^{57}Fe, ^{59}Co, ^{60}Ni, ^{63}Cu, ^{66}Zn, ^{69}Ga, ^{74}Ge, ^{75}As, ^{78}Se, ^{90}Zr, ^{95}Mo, ^{109}Ag, ^{111}Cd, ^{115}In, ^{118}Sn, ^{121}Sb, ^{201}Hg, ^{202}Hg, ^{205}Tl, ^{206}Pb, ^{208}Pb and ^{209}Bi. All data (ppm) was produced with the iolite software package (Paton et al., 2011), using Zn EDX concentrations as internal standards and STD-GL3, NIST-610, NIST-612 and BCR-2G as external standards.

STD-GL3 was used as the primary standard for trace element concentrations. STD-GL3 is a lithium-borate glass containing Zn and Fe sulfide concentrates and a suite of trace elements (Belousov et al., 2023). NIST-610 was used to quantify elements such as Ga that were not available in STD-GL3. Secondary standards NIST-612 and BCR-2G were used to ensure quantification accuracy and precision. With no available external standards containing Tl in wt%, initial traverse concentrations were noticeably lower than EDX measurements. To accommodate this, a correction factor of 2.6 was applied to all Tl concentrations and found to bring the traverses in line with SEM values.

LA-ICP-MS traverses were chosen to simplify displaying simultaneous element correlations. While spot analyses provide elemental concentrations that can be used to indirectly infer correlations, traverses provide direct measurements and correlations across bands over entire samples (eg: Ingles and Mavrogenes, 2021). The Wiesloch sphalerites however are not homogenous and as a result the internal Zn concentrations vary across traverses. While this has no effect on elemental

correlations, accurate concentrations may be less reliable in portions of each traverse.

2.2.3. X-ray fluorescence microscopy and X-ray absorption near edge structure

X-ray fluorescence mapping was conducted at the XFM beamline located at the 3 GeV Australian Synchrotron in Clayton, Victoria, Australia (Paterson et al., 2011; Howard et al., 2020). An incident beam of 18,500 eV was selected by the Si⟨111⟩ horizontal bounce double crystal monochromator and focused to a spot of 2 × 2 μm FWHM using a Kirkpatrick-Baez mirror pair. XRF spectra were collected in event-mode by the annular 384 element Maia detector (Ryan et al., 2010, 2014, 2018) in backscatter geometry. XRF spectra were fit using the Dynamic Analysis technique (Ryan, 2000) implemented in the GeoPIXE software package (Ryan et al., 1990). Such fitting circumvents the interference from close or overlapping emission lines that would be fatal if simply integrating counts within a region of interest. To demonstrate the quality of the fits, examples are presented at the first and last energies on a Tl *L3*-edge XANES spectrum (Appendix A). Notably, the As peaks remain unchanged once Tl fluorescence is excited.

Full XRF spectrum maps were collected by scanning the sample through the beam focus using step sizes between 2 and 20 μm and stage velocities between 2 and 20 μm/s, leading to dwell times between 0.5 and 4 ms/pixel. Map sizes ranged up to 7.2 megapixels, and durations to 80 min/map. Elemental maps were reconstructed from XRF spectra using GeoPIXE software.

XANES stacks of XRF maps were collected for the As *K*-edge at energies between 11,720 and 12,070 eV, with a step-size of 15 eV between 11,720 and 11,855 eV; 1.5 eV between 11,855 and 11,880 eV; 2 eV between 11,880 and 11,900 eV; 5 eV between 11,905 and 11,940 eV; 10 eV between 11,940 and 12,070 eV. Due to time restraints, step sizes were larger than ideal for As XANES, particularly around the white lines of As^{2+} and As^{3+} (11865–11,870 eV). Future As *K*-edge research should
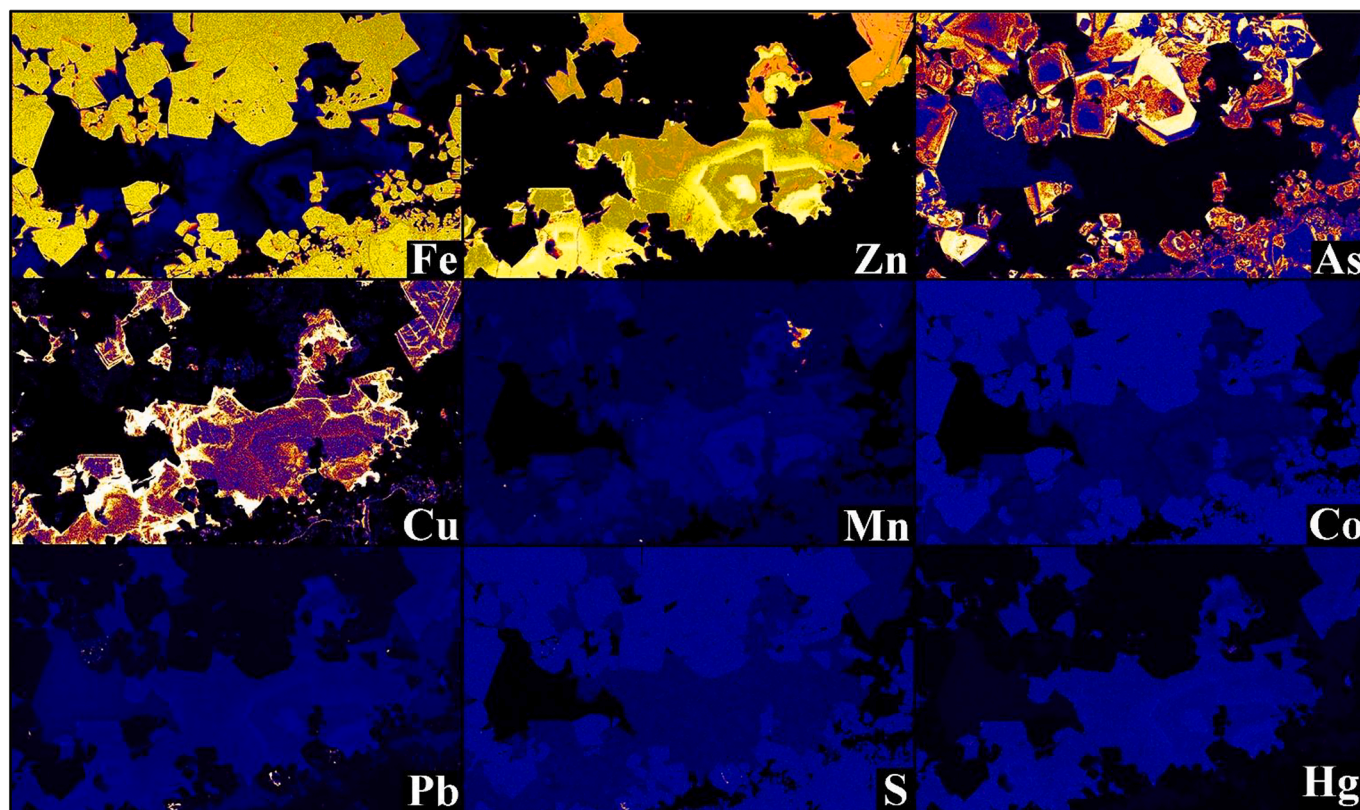
Fig. 5. XFM images showing Fe, Zn, As, Cu, Mn, Co, Pb, S and Hg in pyrite and sphalerite from Porgera, PNG. Warmer colours represent greater concentrations. Pyrite is identifiable by the yellow phases in the Fe image, while sphalerite is most prominent in the Zn image. Arsenic XANES spectra was retrieved from the pyrite with the highest As, visible slightly above centre in the As map. Horizontal scale of 5 mm for each image. (For interpretation of the references to colour in this figure legend, the reader is referred to the web version of this article.)

ensure ≤0.5 eV step sizes over this range to prevent this limitation. The Tl *L3*-edge XANES stacks were collected at energies between 12,495 eV and 12,860 eV, with a step-size of 15 eV between 12,595 and 12,645 eV; 1.5 eV between 12,645 and 12,682 eV; 2 eV between 12,682 and 12,700 eV; 5 eV between 12,700 and 12,740 eV and 10 eV between 12,740 and 12,860 eV.

Across the entire As XANES stacks (101 and 99 scans), dwell times were 3.33 and 4 ms for WIES2 and WIES3 respectively. Any potential beam damage was likely prevented with total exposures of only 0.336 and 0.395 s/pixel. Thallium XANES dwell times were 2 ms across WIES2 and WIES3 XANES stacks (116 and 118 scans respectively). This resulted in 0.232 and 0.236 s/pixel total beam exposure. Regions of interest were selected from the XANES stacks using GeoPIXE, the As or Tl fluorescence intensity summed for the region at each energy of the XANES stack and combined to produce a XANES spectrum and exported to a text file.

XANES spectra were imported into the Athena software package (Ravel and Newville, 2005). Spectra were normalised by fitting a line to pre-edge and third-order polynomial to the post-edge and normalising the edge-step to a value of 1 absorption unit. Normalisation energy clamps were consistent across As and Tl datasets.

3. Results

3.1. Element distribution

Median EDX and LA-ICP-MS concentrations for each of the Wiesloch samples are presented in Table 2. Median data were chosen instead of averages as the results were less influenced by outliers caused by mineral inclusions. Compiled minor and trace element concentrations are also included for each sample as box and whiskers plots (Fig. 2). These results show the lowest Zn and Cd concentrations were accompanied by

the highest As, Tl, Fe, Mn, Sb, Pb and Ge.

Individual EDX analyses, as well as minima, maxima and median concentrations for each of the 15 LA-ICP-MS traverses are included (Appendix B and C). Analyses presented here include higher concentrations of As, Sb, Tl and Pb in Wiesloch sphalerite than reported by Pfaff et al. (2011), likely due to variation across the Wiesloch field and the different stages of mineralisation that each sphalerite contains.

Additional EDX spot analyses are included in Table 3, showing normalised major and minor concentrations traversing sphalerite, galena and a reaction rim. Zinc concentrations increase with proximity to the sphalerite and decreases in sphalerite away from galena. Lead is 10 wt% higher in the reaction rim than the galena, accommodated by decreased concentrations of As and S.

Selected LA-ICP-MS traverses were aligned to sphalerite images (Fig. 3). These traverses reveal differing cation correlations across the coloured bands. For example, As and Tl concentrations in WIES1 increase across the earliest sphalerite zone, while Sb, Pb and Cd decreased, and Fe, Mn, and Co remained constant (Fig. 3A). Comparatively, the final zone in this traverse contained the highest As, Tl, Fe, Mn and Co, and the lowest Sb, Pb and Cd. Interestingly, Ge concentrations were highest in the orange bands in this traverse.

Similarly, the second traverse from WIES1 contained a positive correlation between As and Tl, which also correlated with Ge (Fig. 3B). Iron and Mn correlated in this traverse, with concentrations low in the earliest zones and high in later bands. Comparatively, Pb, Sb and Cd decreased across the entire traverse, with all three depleted in the later growth.

The pitted early growth on both sides of the WIES2 traverse showed low As, Tl, Fe, Mn, Pb and Ge, whereas the later bands were not pitted and contained the highest concentrations of all elements except Sb and Cd (Fig. 3C). Iron and Mn positively correlated again in the WIES3
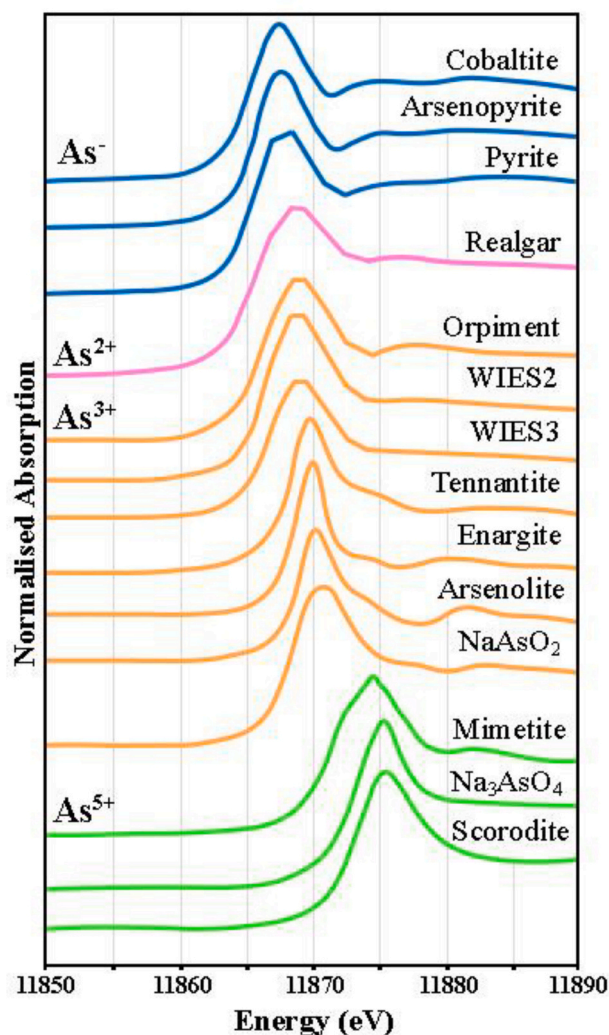
Fig. 6. Arsenic *K*-edge XANES spectra showing sphalerite samples (WIES2–3) and reference standards for different As oxidation states. Results include As *K*-edge spectra measured for this research, as well as Schoepfer et al. (2024) (arsenopyrite, cobaltite, arsenolite and enargite), Diacomanolis et al. (2017) (NaAsO$_2$, Na$_3$AsO$_4$ and scorodite) and Di Benedetto et al. (2011) (tennantite).

traverse, with both elements lowest at the boundaries between the brown and yellow sphalerite (Fig. 3D). Concentrations of Tl, As, Sb, Pb, Cd and Ge in WIES3 were noticeably lowest in the yellow sphalerite.

The localisation of elements in either pitted or non-pitted zones was particularly evident in XFM maps (Fig. 4). In WIES3, Tl was highly concentrated and accompanied by As in two non-pitted bands. Lead was highest in the early Tl zone, while Fe was mostly isolated to the later bands of the sphalerite. A single crossover band between As and Fe was seen in WIES3 (Fig. 4).

Sulfur was homogenous throughout the Wiesloch XFM maps and did not reveal mineral inclusions, however the reaction rim was depicted by S, As, Pb, Cu and Hg concentrations (Fig. 4). The WIES3 XFM maps also confirmed the highest As, Tl, Fe and Pb were accommodated by the lowest Zn concentrations.

XFM mapping was also performed on the Porgera pyrite-sphalerite assemblage (Fig. 5) and WIES2 sphalerite (Appendix D). While WIES2 revealed the same correlations as WIES3, the Porgera sample displayed distinctive zoning in the pyrite and sphalerite. Arsenic was absent from the Porgera sphalerite, but localised in the outer rims of the pyrite, a trend previously documented in pyrite from Porgera and other Papua New Guinea deposits (Peterson and Mavrogenes, 2014; Sykora et al.,

2018).

Comparatively, Zn, Pb and Hg were absent from the Porgera pyrite and highly zoned in the sphalerite (Fig. 5). Iron, Mn and Co furthermore were homogenous in the pyrite and zoned in the sphalerite. Notably, Cu was localised near sphalerite boundaries and crystal defects, except in sphalerite in the top right and top left, where Cu appears to follow cleavage planes. Sulfur was the only homogenous element measured in both sphalerite and pyrite.

Chalcopyrite disease (DIS) was not encountered in any samples by SEM, XFM or LA-ICP-MS traverses. Nor was any evidence of melting from laser ablation.

3.2. XANES

Arsenic *K*-edge spectra (Fig. 6) showed distinct peaks for both sphalerite samples and all measured standards, with an easily visible edge shift for mimetite aligning with the As(V) results of Diacomanolis et al. (2017). Difficulties arose when distinguishing between the divalent and trivalent As in realgar and orpiment spectra respectively, with results showing XANES peaks from both standards extended across 11,868.5 to 11,869.5 eV (Fig. 6 and Appendix E). The first peaks of the first derivatives however aligned the Wiesloch sphalerite with orpiment at 11867 eV, rather than realgar at 11865.5 eV (Fig. 7). This therefore indicates trivalent As in the sphalerite. No inconsistencies were observed in As spectra across bands in WIES2 or WIES3 (Appendix E), verifying a single As oxidation state in the sphalerites.

In contrast, As results from Porgera pyrite (Fig. 6) closest resemble the anionic arsenopyrite and cobaltite *K*-edge XANES spectra from Schoepfer et al. (2024). This indicates that As$^-$ is occupying S sites, as per the natural pyrites analysed by Le Pape et al. (2018).

Thallium *L3*-edge spectra for WIES2 and WIES3 sphalerites and the two measured Tl standards produced the same featureless shape that spanned 12,650–12,680 eV (Fig. 8). This S-shaped curve is common in monovalent Tl *L3*-edge XANES spectra and differs from the hump seen in Tl(III) compounds (Fig. 8; Agarwal and Vishnoi, 2005; George et al., 2019; Garrido et al., 2020; Łyczko et al., 2023). Edge energies of 12,663.5 eV were also retrieved from Athena software for the sphalerite, lorándite and Tl(I)-silicate, confirming Tl$^+$ in WIES2 and WIES3. Despite some noise in Tl XANES results, the spectra were consistent between the sphalerites and multiple analyses from the Tl-silicate and lorándite (Appendix E).

Pre-edge features were absent from As *K*-edge and Tl *L3*-edge spectra, likely due to the filled 3d and 5d orbitals respectively.

4. Discussion

4.1. Oxidation states of Tl and As

In our As XANES results (Fig. 6), a considerable edge shift (5.5 eV) was evident between the Wiesloch sphalerite and the pentavalent spectra from mimetite. This correlates with similar observations of pentavalent arsenate XANES spectra (Charnock et al., 2007; Diacomanolis et al., 2017) and eliminates As^{5+} as a possibility in Wiesloch sphalerite. While divalent and trivalent As XANES spectra can be difficult to distinguish in sulfides (Qian et al., 2013; Le Pape et al., 2018; Saurette et al., 2022), the first peaks of the first derivatives were used to resolve the different valence species (Fig. 7). Noticeably, the first peaks of the first derivatives align sphalerite with orpiment rather than realgar and therefore confirmed trivalent As in the Wiesloch sphalerite.

With XFM maps showing a sphalerite-pyrite mineral assemblage and As solely in the pyrite (Fig. 5), it is possible that As partitioning between two coprecipitating mineral pairs is redox dependent. Trace concentrations may therefore provide a pH estimate of the mineralising fluid, where As is localised exclusively in pyrite or sphalerite. Ferguson and Gavis (1972) found realgar and orpiment were separated below and above pH 3–4 respectively. Pyrite and sphalerite may therefore also
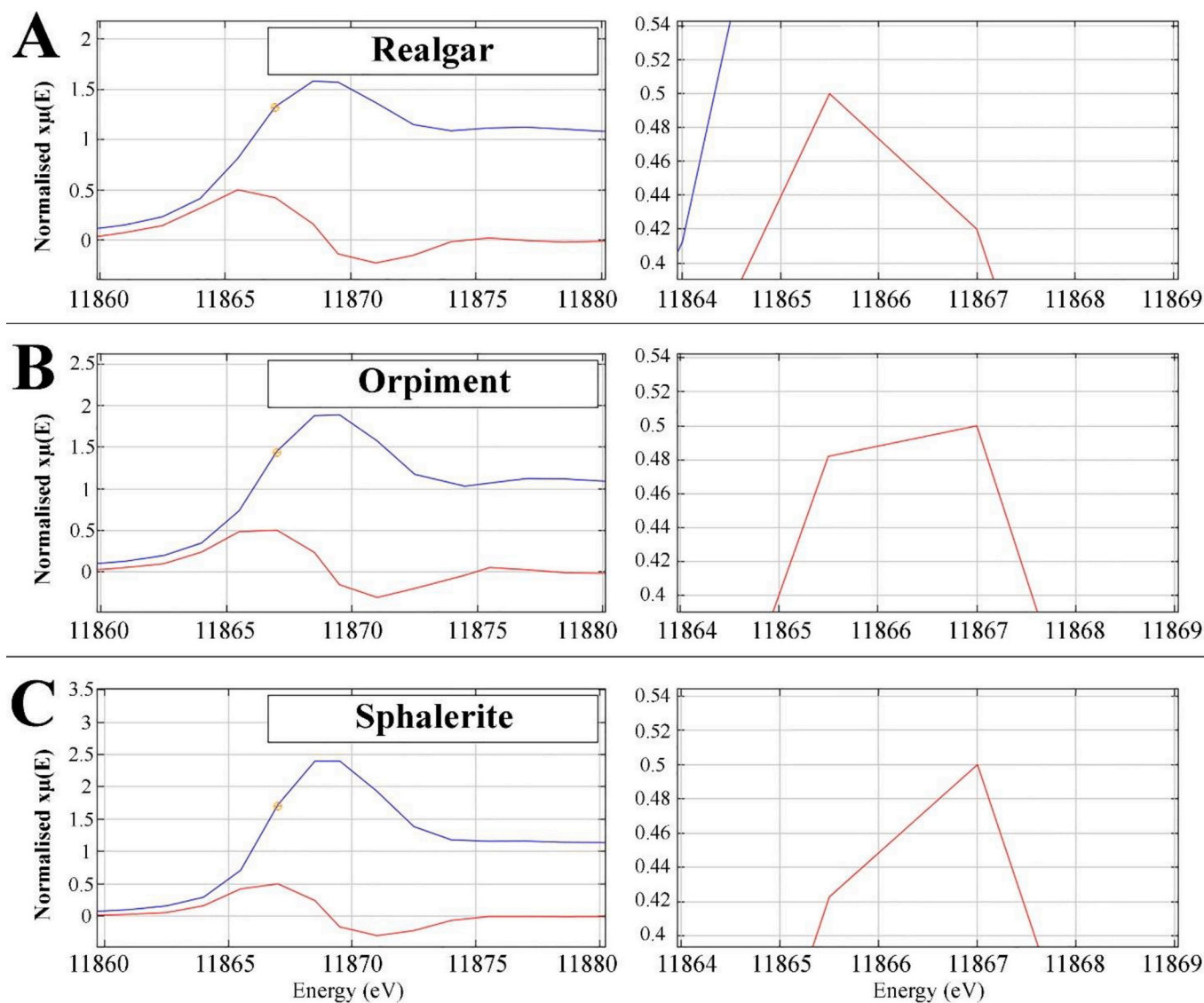
Fig. 7. Left: Comparison of As *K*-edge XANES (blue) and corresponding first derivative spectra (red). Right: The first derivatives reveal a realgar (A) peak at 11865.5 eV, and orpiment (B) and sphalerite (C) at 11867 eV. (For interpretation of the references to colour in this figure legend, the reader is referred to the web version of this article.)

reflect a pH boundary when only one phase in a coprecipitating assemblage contains As. This would also imply trivalent As in all MVT sphalerites, as the carbonate hosting minerals would buffer pH.

Confidence of Tl^+ in the Wiesloch sphalerite is supported by the Tl XANES of previous research (Fig. 8). This demonstrates the edge shift and shape change associated with trivalent Tl *L3*-edge spectra (eg: Voegelin et al., 2015; George et al., 2019; Wick et al., 2019) and is highlighted by direct comparisons of Tl(I) and Tl(III) in aqueous solutions and organic compounds (Agarwal and Vishnoi, 2005; Garrido et al., 2020; Łyczko et al., 2023).

4.2. Substitution Mechanisms

LA-ICP-MS traverses and XFM maps show As—Tl correlations in the Wiesloch sphalerite, with both cations also inversely correlated to Pb (Fig. 3A) and Fe (Fig. 3B). Consistent As—Tl correlations independent of other elements, plus the affinity that both cations share for low temperature mineralisation therefore supports the joint incorporation of As and Tl in Wiesloch sphalerite. Furthermore, a formula can be constructed with this coupled substitution, with two Zn^{2+} trading for one

Tl^+ and one As^{3+}:

$$2Zn^{2+} \longleftrightarrow Tl^+ + As^{3+} \tag{1}$$

Arsenic concentrations however exceed Tl in many EDX and LA-ICP-MS results, indicating at least minor incorporation of As independently of Tl. With other monovalent cations unavailable to pair with, such as Cu^+ and Ag^+, sole substitution of As^{3+} for Zn^{2+} must occur. Different oxidation states on the two cations dictate the stoichiometry will be balanced with a vacant site:

$$3Zn^{2+} \longleftrightarrow 2As^{3+} + \square \tag{2}$$

Interestingly, vacancies produced from the incorporation of As may be expressed in the Wiesloch sphalerite by the pitted textures (Figs. 1, 3 and 4). Pits are only visible within low Tl-bands, where they may reflect open spaces such as vacancies within the lattice. XFM imagery (Fig. 4 and Appendix D) shows Tl is concentrated within the non-pitted bands and this may suggest Tl is occupying the vacant sites created by As substitution.

An alternative explanation for high-Tl, non-pitted bands could be Tl-inclusions occupying formerly pitted sites exclusively within these
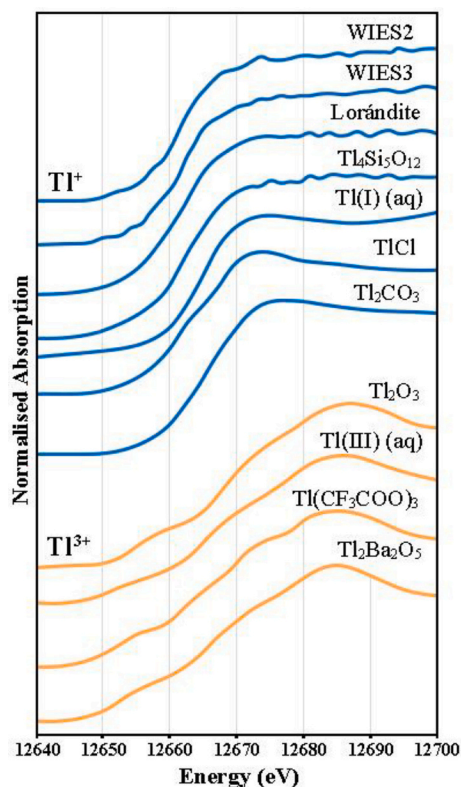
Fig. 8. Thallium *L3*-edge XANES spectra showing sphalerite samples (WIES2–3) and reference standards for different Tl oxidation states. Results include Tl *L3*-edge spectra measured for this research, as well as Agarwal and Vishnoi (2005) (TlCl, Tl_2CO_3, $Tl(CF_3COO)_3$ and $Tl_2Ba_2O_5$), Garrido et al. (2020) (aqueous Tl^+ and Tl_2O_3) and Łyczko et al. (2023) (aqueous Tl^{3+}).

bands however these inclusions would be visible in XFM and LA-ICP-MS. Additionally, the XFM maps and EDX results show that S concentrations are constant across all sphalerite bands, with elevated concentrations of Fe, As and Tl accommodated by proportionally decreased Zn and Cd concentrations. Instead, larger cations such as Tl^+ could be localised in energetically favourable bands, aided into the lattice by vacancies. A substitution equation with Zn^{2+} and a vacant site substituting for two Tl^+ cations:

$$Zn^{2+} + \square \leftarrow\rightarrow 2Tl^+ \tag{3}$$

This formula effectively utilises the initial vacancy created from the As equation and may act as a second step in a substitutional chain.

Combining the previous two equations creates a single vacant site on either side of a reaction:

$$4Zn^{2+} + \square \leftarrow\rightarrow 2Tl^+ + 2As^{3+} + \square \tag{4}$$
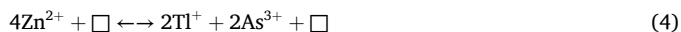
Where cancelling out the vacancies and dividing the cations by 2, results in the initial proposed coupled substitution of two Zn^{2+} for one Tl^+ and one As^{3+} (Eq. (1)).

Substitution of larger cations, such as Tl^+ (>1 Å), into sphalerite is contentious as their size exceeds Goldschmidt substitution rules, which supports simple substitution within 30 % of Zn^{2+} in tetrahedral coordination. Often the presence of these elements is explained as micro- or nano-inclusions of other minerals. Pring et al. (2008) however demonstrated the flexibility of the S^{2-} electron cloud, which can readily distort and accommodate larger cations in the lattice without significant lattice strain. Further investigations by Pring et al. (2020) also confirmed sphalerite as the most favourable ZnS polymorph to contain larger cations.

While Eq. (1) sufficiently explains the coupled substitution of As and Tl into the sphalerite lattice, it does not address the large size of Tl^+ or the preferential nature of the cation deficient polymorph to incorporate vacant sites (Scott and Barnes, 1972). Eqs. (2 and 3) therefore, could better explain the substitution by creating and consuming vacancies respectively. Eq. (4) furthermore, depicts these two processes as one reaction.

Interestingly, the average crystal radii of Tl^+ and As^{3+} combined brings Tl^+ closer to Goldschmidt expectations. This supports the presence of other large cations in the sphalerite lattice, for example Ag^+, when it is paired with smaller cations such as As^{3+}, Ga^{3+} or Sn^{4+}. Whether vacancies and multiple stages are required for the incorporation of cations requires further investigation, including whether each step would occur near simultaneously or involve additional processes such as diffusion.

5. Conclusions

The XANES results presented here indicate monovalent Tl and trivalent As in Wiesloch sphalerite. Results further suggest anionic As^- in Porgera pyrite. Additionally, in equilibrium sphalerite-pyrite assemblages, redox may control As partitioning between sulfides. This could also indicate trace concentrations of As reveal a pH boundary similar to that previously established by As in realgar and orpiment.

The incorporation of Tl in sphalerite may be solely due to coupled substitution with As or both cations could enter the lattice independently, where one precedes the other in a two-step substitution. Firstly, incorporation of As in sphalerite creates a vacancy, which may subsequently be used by Tl. Furthermore, combining these two equations and cancelling out the vacant sites creates a formula equivalent to the initial coupled substitution.

CRediT authorship contribution statement

Christopher H. Ingles: Writing – original draft, Visualization, Methodology, Investigation, Formal analysis, Data curation, Conceptualization. **John A. Mavrogenes:** Writing – review & editing, Supervision, Methodology, Investigation, Conceptualization. **Nicholas D. Tailby:** Writing – review & editing, Methodology, Investigation. **Jeremy L. Wykes:** Writing – review & editing, Methodology, Investigation.

Declaration of competing interest

The authors declare that they have no known competing financial interests or personal relationships that could have appeared to influence the work reported in this paper.

Data availability

Data are available through Mendeley Data at https://doi.org/10.17632/c4n63vbzrb.1

Appendix A

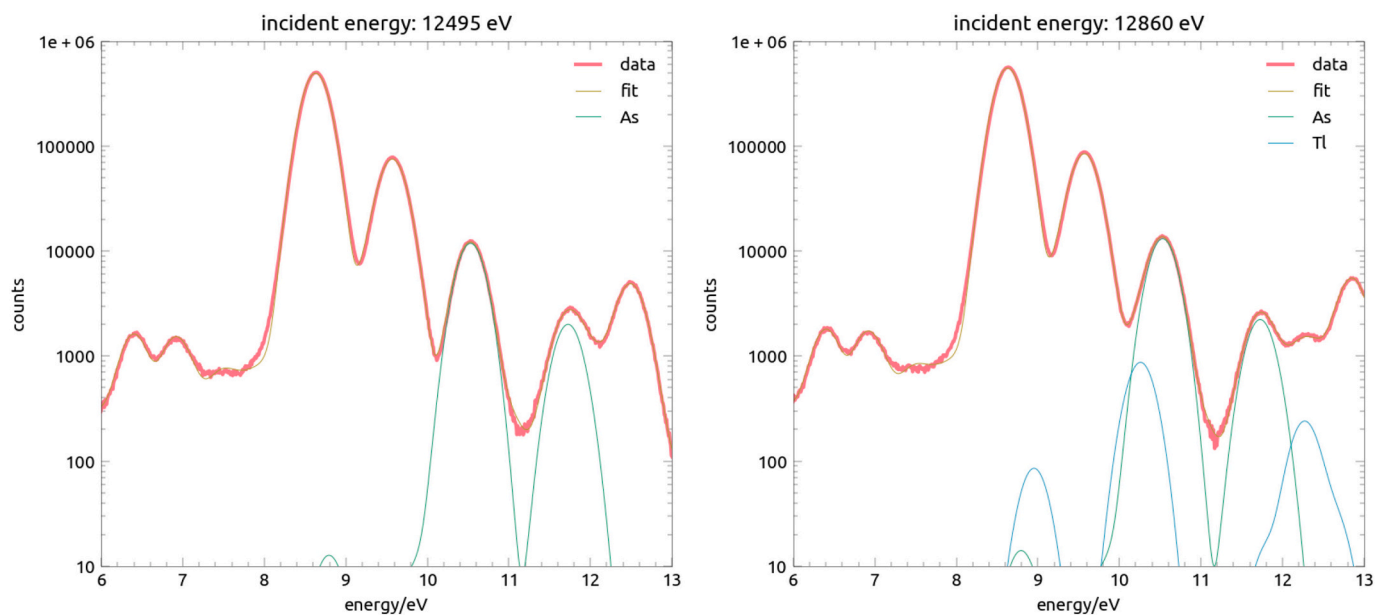**Fig. A.1.** The first (left) and last (right) energies on a Tl *L3*-edge XANES spectrum. Once Tl fluorescence is excited, As peaks remain unchanged.

Appendix B

Table B.1
FE-SEM spot analyses (wt%) from WIES1-3. Concentrations not included were below detection limits (0.1 wt%).

Sample	Spot	Zn	S	Fe	Cd	As	Tl	Sb	Pb	Total
WIES1	Spot 1	62.75	31.86	1.04	–	1.69	1.46	–	1.60	100.40
	Spot 2	63.32	32.37	1.26	–	1.67	1.52	–	1.45	101.60
	Spot 3	64.82	32.94	2.26	–	–	–	–	–	100.03
	Spot 4	63.49	32.15	0.81	–	1.84	1.35	–	1.91	101.55
	Spot 5	61.26	30.76	0.32	–	1.85	1.53	0.36	2.82	98.91
	Spot 6	62.48	31.07	–	–	1.49	1.09	0.37	2.69	99.19
	Spot 7	63.99	31.76	–	–	0.86	–	0.45	3.11	100.16
	Spot 8	63.89	31.43	–	–	0.76	–	0.33	2.66	99.07
	Spot 9	59.86	30.80	–	0.22	2.38	1.91	0.30	3.97	99.45
	Spot 10	60.76	30.64	0.28	–	1.93	1.48	0.64	3.67	99.41
	Spot 11	61.01	31.21	0.34	0.24	1.95	1.44	0.35	3.33	99.87
	Spot 12	62.01	30.61	–	–	0.66	1.93	0.75	2.40	98.36
WIES2	Spot 1	63.61	31.24	–	–	1.49	1.25	–	2.14	99.73
	Spot 2	63.58	31.16	–	–	1.14	1.63	–	1.50	99.02
	Spot 3	61.40	30.52	–	–	1.26	–	0.91	3.90	97.99
	Spot 4	65.28	31.34	–	–	–	1.15	0.27	1.11	99.15
	Spot 5	66.09	31.94	–	–	–	1.33	0.25	1.09	100.70
	Spot 6	66.58	32.11	–	0.25	–	–	–	1.08	100.02
WIES3	Spot 1	63.93	31.93	–	–	0.51	–	0.47	2.43	99.28
	Spot 2	65.15	31.55	–	–	0.37	–	0.38	1.84	99.30
	Spot 3	64.97	31.72	–	0.30	0.61	–	0.25	2.18	100.03
	Spot 4	65.94	32.05	–	0.38	0.31	–	0.43	2.22	101.33
	Spot 5	64.91	31.77	–	0.36	0.64	–	0.40	2.25	100.32
	Spot 6	62.31	31.18	0.17	–	1.84	1.52	–	2.95	99.98
	Spot 7	64.65	31.73	–	–	1.31	1.15	–	2.59	101.42

Appendix C

Table C.1
Table of minimum, maximum and median concentrations from each LA-ICP-MS traverse (ppm). Concentrations below 0.1 ppm reported as BDL (Below Detection Limits).

| Sample	Traverse	Data Type	Mn (ppm)	Fe (ppm)	Co (ppm)	Cu (ppm)	Ge (ppm)	As (ppm)	Cd (ppm)	Sb (ppm)	Tl (ppm)	Pb (ppm)
WIES1	1	Min	3.8	139.6	0.1	0.8	13.7	6128.7	6.8	538.9	4292.3	16,024.2
		Max	37.8	3458.2	8.0	4.9	94.4	14,662.7	1291.2	6803.8	19,291.6	28,273.6
		Median	7.1	246.6	0.7	2.5	32.8	9524.8	902.5	4193.1	6655.8	23,573.1
	2	Min	5.0	156.4	BDL	0.4	8.1	547.0	3.9	147.6	561.4	1501.4
		Max	33.6	7869.0	13.6	14.0	75.3	13,953.4	1697.0	10,139.8	18,016.7	39,265.5
		Median	13.7	1071.4	0.6	2.5	26.9	7516.2	184.6	1882.3	5589.8	15,559.1
WIES2	1	Min	4.1	165.0	0.2	0.4	10.6	3322.8	66.3	804.7	4756.6	13,193.8
		Max	26.9	1209.0	2.6	8.0	91.2	17,094.6	1718.0	9074.2	16,503.4	49,502.8
		Median	8.3	433.5	0.8	2.2	33.2	9590.0	674.3	3104.4	7728.5	21,711.8
	2	Min	5.1	161.7	BDL	1.2	7.8	3026.8	90.4	822.3	4085.4	13,909.3
		Max	22.0	1161.4	1.8	6.9	93.0	15,918.2	1481.5	9353.8	14,201.2	55,201.6
		Median	8.3	357.3	0.7	3.5	31.9	9071.2	910.0	3829.5	6943.2	22,330.8
	3	Min	3.3	120.3	0.1	0.5	2.0	702.6	173.5	766.1	440.7	5575.6
		Max	25.6	1161.6	2.3	5.5	44.2	15,143.4	2351.5	3965.4	15,180.1	27,004.6
		Median	5.4	192.1	0.6	1.9	6.7	1586.2	1220.3	2204.5	901.9	8283.0
	4	Min	1.6	77.1	BDL	1.1	3.9	1375.0	346.6	842.0	758.1	9474.1
		Max	34.3	1418.3	2.1	6.5	56.9	17,541.5	2014.9	6157.5	17,417.5	48,004.3
		Median	3.7	161.3	0.7	3.3	23.7	2364.9	769.1	3129.0	3553.9	14,487.3
WIES3	1	Min	1.71	64.3	BDL	1.1	1.6	315.3	0.9	131.8	218.1	3365.5
		Max	39.9	8670.0	17.5	11.2	49.5	16,136.5	2263.2	4996.9	16,950.7	28,057.9
		Median	5.2	176.7	0.6	3.0	18.1	2934.5	1686.2	2629.7	4924.8	14,849.5
	2	Min	2.1	87.9	BDL	0.1	1.8	709.2	1.9	162.1	439.3	3154.5
		Max	30.3	8417.0	16.3	23.8	48.7	15,914.4	2042.1	3131.3	17,200.7	28,520.4
		Median	6.1	269.8	0.6	1.6	10.6	1610.1	469.9	1002.1	2859.2	7340.2
	3	Min	2.0	72.1	BDL	0.5	5.1	1249.4	2.3	140.9	610.6	3073.7
		Max	42.6	9443.2	15.9	23.4	45.7	18,107.1	1306.4	3245.1	17,983.0	32,998.4
		Median	13. 2	575.4	0.7	2.5	22.3	2583.3	369.4	902.8	5105.8	9181.5
	4	Min	2.9	93.3	BDL	1.5	3.3	1131.9	2.9	133.3	617.3	3170.0
		Max	33.5	9018.6	15.3	20.1	48.6	16,614.0	1234.5	2724.2	16,246.2	26,767.2
		Median	12.5	556.2	0.7	3.6	22.9	2490.1	294.9	830.8	4970.9	7910.7
	5	Min	0.5	46.2	0.1	0.7	4.7	437.3	374.2	725.9	783.9	4520.2
		Max	31.4	976.2	1.9	13.5	81.5	12,005.4	1830.8	4359.7	12,830.1	31,729.2
		Median	8.8	370.4	0.7	2.7	25.9	9177.3	988.3	2979.9	7100.0	19,086.7
	6	Min	2.7	86.6	BDL	BDL	5.5	1525.5	1.7	159.9	1043.5	3192.7
		Max	37.6	8953.1	15.7	8.1	86.4	14,044.6	1744.8	6448.9	18,140.5	58,730.3
		Median	7.0	252.1	0.7	1.9	27.0	3631.0	589.3	3211.1	4901.8	18,385.5
	7	Min	2.1	61.7	BDL	0.4	1.9	449.7	798.5	1985.9	328.3	6650.2
		Max	29.6	605.6	1.6	14.4	79.6	15,678.2	2338.0	5689.4	13,051.8	31,126.9
		Median	5.1	170.1	0.5	2.6	12.9	2112.8	1742.2	3246.5	3606.2	15,523.8
	8	Min	1.5	46.1	BDL	0.9	0.4	244.9	1199.0	425.4	188.3	3217.9
		Max	18.7	348.3	1.4	5.5	22.8	7276.0	2302.1	5363.9	6204.6	29,801.0
		Median	3.9	125.8	0.5	2.4	12.3	2004.9	1835.0	3716.0	2520.4	15,284.6
	9	Min	2.0	57.5	BDL	0.8	13.1	1711.2	1513.4	2484.9	2981.9	10,198.8
		Max	5.3	138.3	1.2	4.7	25.3	3496.6	2071.8	5346.5	6639.6	25,771.2
		Median	2.9	87.3	0.5	2.5	17.9	2562.9	1714.9	3601.4	4528.3	17,198.2

Appendix D
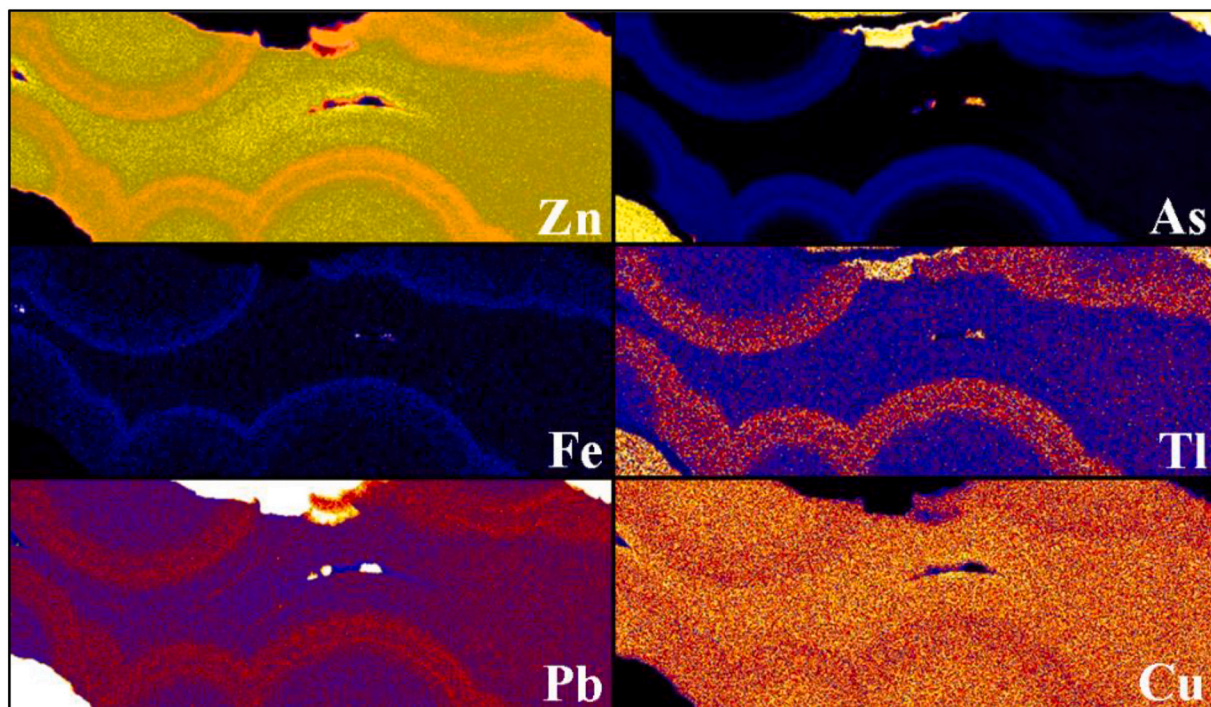
Fig. D.1. XFM images showing Zn, As, Fe, Tl, Pb and Cu in sphalerite in WIES2. Warmer colours represent greater concentrations. Galena is visible in all images protruding in on the top centre, top right and bottom left of each frame.
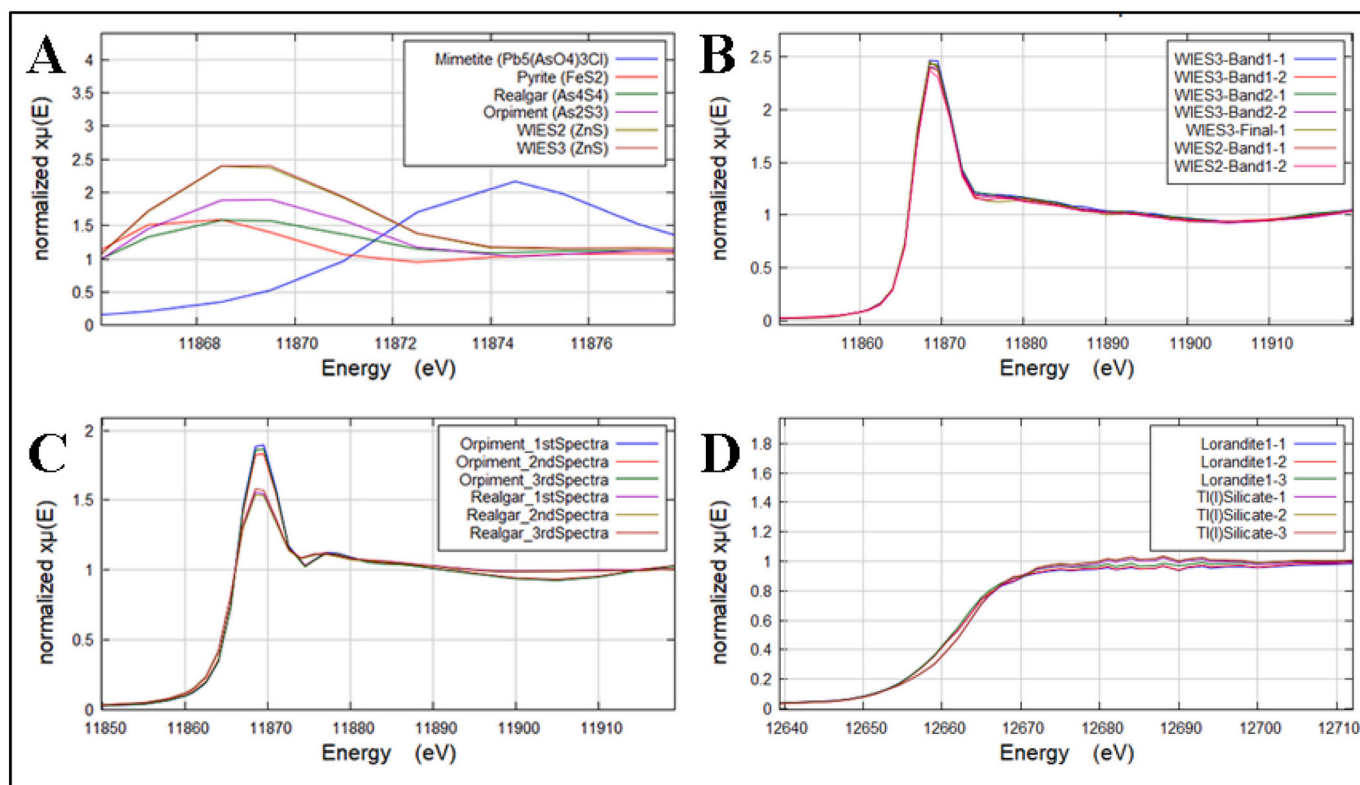
Appendix E

Fig. E.1. Comparison of As *K*-edge and Tl *L3*-edge XANES spectra. A) A close-up between mimetite (right) and the other As standards, pyrite and sphalerite (left). B) Arsenic spectra from different bands in WIES2 and WIES3 sphalerite. C) Arsenic spectra from different orpiment and realgar regions. D) Spectra from different regions in the Tl standards.

References

Agarwal, A., Vishnoi, A., 2005. XANES studies of thallium compounds and valence states and local environment of thallium in some of its superconducting cuprates. Phys. Scr. T115, 534–537.

Barton, P., Bethke, P., 1987. Chalcopyrite disease in sphalerite; pathology and epidemiology. Am. Mineral. 72 (5–6), 451–467.

Belissont, R., Munoz, M., Boiron, M., 2016. Distribution and oxidation state of Ge, Cu and Fe in sphalerite by μ-XRF and K-edge μ-XANES: insights into Ge incorporation, partitioning and isotopic fractionation. Geochim. Cosmochim. Acta 177, 298–314.

Belousov, I., Danyushevsky, L., Geomann, K., Gilbert, S., 2023. STDGL3, a Reference Material for Analysis of Sulfide Minerals by Laser Ablation ICP-MS : an Assessment of Matrix Effects and the Impact of Laser Wavelengths and Pulse Widths. Geostand. Geoanal. Res. 47 (3), 493–508.

Burton, J., 2022. 2022 Final List of Critical Minerals, U.S. Geological Survey, U.S. Department of the Interior. Federal Government of the United States.

Chareev, D., Osadchii, V., Shiryaev, A., 2017. Single-crystal Fe-bearing sphalerite: synthesis, lattice parameter, thermal expansion coefficient and microhardness. Phys. Chem. Miner. 44, 287–296.

Charnock, J., Polya, D., Gault, A., Wogelius, R., 2007. Direct EXAFS evidence for incorporation of As5+ in the tetrahedral site of natural andraditic garnet. Am. Mineral. 92 (11–12), 1856–1861.

Clark, A., 1970. Arsenian sphalerite from Mina Alcaran, Pampa Larga, Copiapó, Chile. Am. Mineral. 55 (9–10), 1794–1797.

Cook, N., Ciobanu, C., Pring, A., 2009. Trace and minor elements in sphalerite: a LA-ICPMS study. Geochim. Cosmochim. Acta 73, 4761–4791.

Cook, N., Ciobanu, C., Brugger, J., Etschmann, B., 2012. Determination of the oxidation state of Cu in substituted Cu-In-Fe-bearing sphalerite via μ-XANES spectroscopy. Am. Mineral. 97 (2–3), 476–479.

Di Benedetto, F., Da Pelo, S., Caneschi, A., Lattanzi, P., 2011. Chemical state of arsenic and copper in enargite: evidences from EPR and X-ray absorption spectroscopies, and SQUID magnetometry. N. Jb. Mineral. (Abh.) 188, 11–19.

Diacomanolis, V., Noller, B., Taga, R., 2017. Relationship of arsenic speciation and bioavailability in mine wastes for human health risk assessment. Environ. Chem. 13 (4), 641–655.

Dordevic, T., Drahota, P., Kolitsch, U., 2021. Synergetic Tl and as retention in secondary minerals: an example of extreme arsenic and thallium pollution. Appl. Geochem. 135, 105114.

Ferguson, J., Gavis, J., 1972. A review of the arsenic cycle in natural waters. Water Res. 6 (11), 1259–1274.

Frenzel, M., Hirsch, T., Gutzmer, J., 2016. Gallium, germanium, indium, and other trace and minor elements in sphalerite as a function of deposit type — a meta-analysis. Ore Geol. Rev. 76, 52–78.

Garrido, F., Garcia-Guinea, J., Lopez-Arce, P., 2020. Thallium and co-genetic trace elements in hydrothermal Fe-Mn deposits of Central Spain. Sci. Total Environ. 717, 137162.

George, M., 2023. Mineral Commodity Summaries – Arsenic, January. U.S. Geological Survey, p. 2023.

George, L., Biagioni, C., Lepore, G., Lacalamita, M., 2019. The speciation of thallium in (Tl,Sb,As)-rich pyrite. Ore Geol. Rev. 107, 364–380.

Govindarao, B., Pruseth, K., Mishra, B., 2018. Sulfide partial melting and chalcopyrite disease: an experimental study. Am. Mineral. 103 (8), 1200–1207.

Grohol, M., Veeh, C., 2023. Study on the Critical Raw Materials for the EU 2023. Publications Office of the European Union, Directorate-General for Internal Market, Industry, Entrepreneurship and SMEs, European Commission.

Howard, D., de Jonge, M., Afshar, N., 2020. The XFM beamline at the Australian Synchrotron. J. Synchrotron Radiat. 27, 1447–1458.

Ikramuddin, M., Besse, L., Nordstrom, P., 1986. Thallium in the Carlin-type gold deposits. Appl. Geochem. 1, 493–502.

Ingles, C., Mavrogenes, J., 2021. Cationic substitutions in sphalerite from the Porgera mine, Papua New Guinea. Can. Mineral. 59 (3), 573–587.

Karbowska, B., Zembrzuski, W., Jakubowska, M., 2014. Translocation and mobility of thallium from zinc–lead ores. J. Geochem. Explor. 143, 127–135.

King, M., 2023. Government Backs Critical Minerals for Energy, Jobs and Defence, Department of Industry, Science and Resources, Media Release (16 December 2023).

Le Pape, P., Blanchard, M., Amelie, J., Jean-Pascal, R., Manoj, D., Guillaume, M., Delphine, V., 2018. Local environment of arsenic in sulfide minerals: insights from high-resolution X-ray spectroscopies, and first-principles calculations at the as K-edge. J. Anal. At. Spectrom. 33, 2070.

Łyczko, K., Więckowska, A., Bajnoczi, E., Csupasz, T., Purgel, M., Clauss, K., Toth, I., Persson, I., 2023. Striking stability of a mixed-valence thallium(III)-thallium(I) complex in some solvents. J. Mol. Liq. 385, 122233.

Mavrogenes, J., Hagni, R., Dingess, P., 1992. Mineralogy, Paragenesis, and Mineral Zoning of the West Fork Mine, Viburnum Trend, Southeast Missouri. Econ. Geol. 87 (1), 113–124.

Paterson, D., de Jonge, M., Howard, D., Lewis, W., 2011. The X-ray fluorescence microscopy beamline at the Australian synchrotron. AIP Conf. Proc. 1365, 219.

Paton, C., Hellstrom, J., Paul, B., Woodhead, J., 2011. Iolite: Freeware for the Visualisation and Processing of Mass Spectrometric Data. J. Anal. At. Spectrom. 26, 2508–2518.

Peterson, E., Mavrogenes, J., 2014. Linking high-grade gold mineralization to earthquake-induced fault-valve processes in the Porgera gold deposit, Papua New Guinea. Geology 42 (5), 383–386.

Pfaff, K., Hildebrandt, L., Leach, D., Jacob, D., Markl, G., 2010. Formation of the Wiesloch Mississippi Valley-type Zn-Pb-Ag. Mineral. Deposita 45, 647–666.

Pfaff, K., Koenig, A., Wenzel, T., Ridley, I., 2011. Trace and minor element variations and sulfur isotopes in crystalline and colloform. Chem. Geol. 286, 118–134.

Pring, A., Tarantino, S., Tenailleau, C., 2008. The crystal chemistry of Fe-bearing sphalerites: an infrared spectroscopic study. Am. Mineral. 93, 591–597.

Pring, A., Wade, B., McFadden, A., 2020. Coupled substitutions of minor and trace elements in co-existing sphalerite and wurtzite. Minerals 10, 147.

Qian, G., Brugger, J., Testemale, D., Skinner, W., Pring, A., 2013. Formation of as(II)-pyrite during experimental replacement of magnetite under hydrothermal conditions. Geochim. Cosmochim. Acta 100, 1–10.

Ravel, B., Newville, M., 2005. Athena, Artemis, Hephaestus: data analysis for X-ray absorption spectroscopy using IFEFFIT. J. Synchrotron Radiat. 12, 537–541.

Ryan, C., 2000. Quantitative trace element imaging using PIXE and the nuclear microprobe. Int. J. Imaging Syst. Technol. 11, 219–230.

Ryan, C., Cousens, D., Sie, S., Griffin, W., Suter, G., Clayton, E., 1990. Quantitative pixe microanalysis of geological matemal using the CSIRO proton microprobe. Nucl. Inst. Methods Phys. Res. B 47, 55–71.

Ryan, C., Kirkham, R., Hough, R., Moorhead, G., Siddons, D., 2010. Elemental x-ray imaging using the maia detector array: the benefits and challenges of large solid-angle. Nucl. Instrum. Meth. A 619 (1–3), 37–43.

Ryan, C., Siddons, D., Kirkham, R., Li, Z., de Jonge, M., Paterson, D., 2014. Maia X-ray fluorescence imaging: Capturing detail in complex natural samples. J. Phys. Conf. Ser. 499, 012002.

Ryan, C., Kirkham, R., de Jonge, M.D., Siddons, D.P., van der Ent, A., Pagés, A., 2018. The Maia Detector and Event Mode. Synchrotron Radiat. News 31 (6), 21–27.

Rytuba, J., 1986. Arsenic minerals as indicators of conditions of gold deposition in Carlin-type gold deposits. J. Geochem. Explor. 25, 237–238.

Saurette, E., Finfrock, Y., Verbuyst, B., Blowes, D., 2022. Improved precision in as speciation analysis with HERFD-XANES at the as K-edge: the case of as speciation in mine waste. J. Synchrotron Radiat. 29, 5.

Schoepfer, V., Jamieson, H., Lindsay, M., 2024. Arsenic mineral and compound data as analyzed by X-ray absorption spectroscopy and X-ray diffraction. Data in Brief 55, 110634.

Scott, S., 1973. Experimental calibration of the sphalerite geobarometer. Econ. Geol. 68 (4), 466–474.

Scott, S., Barnes, H., 1971. Sphalerite geothermometry and geobarometry. Econ. Geol. 66, 653–669.

Scott, S., Barnes, H., 1972. Sphalerite-wurtzite equilibria and stoichiometry. Geochim. Cosmochim. Acta 36, 1275–1295.

Shannon, R., 1976. Revised effective ionic radii and systematic studies of interatomic distances in halides and chalcogenides. Acta Crystallogr. 32, 751–767.

Singh, M., 2022. Mineral Commodity Summaries – Thallium, January. U.S. Geological Survey, p. 2022.

Stüben, D., Berner, Z., Kappes, B., Puchelt, H., 2001. Environmental monitoring of heavy metals and arsenic from Ag-Pb-Zn mining. Environ. Monit. Assess. 70, 181–200.

Sykora, S., Cooke, D., Meffre, S., Stephanov, A., Gardner, K., Scott, R., Selley, D., Harris, A., 2018. Evolution of Pyrite Trace Element Compositions from Porphyry-style and Epithermal Conditions at the Lihir Gold Deposit: Implications for Ore Genesis and Mineral Processing. Econ. Geol. 113, 193–208.

Tabelin, C., Igarishi, T., 2009. Mechanisms of arsenic and lead release from hydrothermally altered rock. J. Hazard. Mater. 169, 980–990.

Voegelin, A., Pfenninger, N., Petrikis, J., Majzlan, J., Plötze, M., Senn, A.-C., Mangold, S., Steininger, R., Göttlicher, J., 2015. Thallium speciation and extractability in a thallium- and arsenic-rich soil developed from mineralized carbonate rock. Environ. Sci. Technol. 49, 5390–5398.

Wick, S., Pena, J., Voegelin, A., 2019. Thallium Sorption onto Manganese Oxides. Environ. Sci. Technol. 53 (22), 13168–13178.

Wright, K., Gale, J., 2010. A first principles study of the distribution of iron in sphalerite. Geochim. Cosmochim. Acta 12, 3514–3520.

Ye, L., Cook, N., Ciobanu, C., 2011. Trace and minor elements in sphalerite from base metal deposits in South China: a LA-ICPMS study. Ore Geol. Rev. 39, 188–217.

Yu, H., Li, M., Wang, W., Wang, X., 2016. High throughput screening technologies for ion channels. Acta Pharmacol. Sin. 37, 34–43.

Zhao, F., Gu, S., 2021. Secondary Sulfate Minerals from Thallium Mineralized areas: their Formation and Environmental significance. Minerals 11, 855.

Zhou, Y., He, H., Wang, J., 2022. Stable isotope fractionation of thallium as novel evidence for its geochemical transfer during lead-zinc smelting activities. Sci. Total Environ. 803, 150036.